Discrete Elemental Distributions inside a Single Mixed-Halide Perovskite Nanocrystal for the Self-Assembly of Multiple Quantum-Light Sources

Jinqiu Liu,[@] Chao Zhu,*,[@] Mike Pols,[@] Zhen Zhang,[@] Fengrui Hu, Lin Wang, Chunfeng Zhang, Zheng Liu, Shuxia Tao,* Min Xiao,* and Xiaoyong Wang*

Cite This: Nano Lett. 2023, 23, 10089−10096

Read Online

ACCESS | ll Metrics & More | Article Recommendations | SI Supporting Information

ABSTRACT: An in-depth understanding of the structure−property relationships in semiconductor mixed-halide perovskites is critical for their potential applications in various light-absorbing and light-emitting optoelectronic devices. Here we show that during the crystal growth of mixed-halide $CsPbBr_{1.2}I_{1.8}$ nanocrystals (NCs), abundant Ruddlesden−Popper (RP) plane stacking faults are formed to release the lattice strain. These RP planes hinder the exchange of halide species across them, resulting in the presence of multiple nanodomains with discrete mixed-halide compositions inside a single $CsPbBr_{1.2}I_{1.8}$ NC. Photoluminescence peaks from these pre-segregated nanodomains, whose correlated intensity and wavelength variations signify the interactions of coupled quantum dots within a single $CsPbBr_{1.2}I_{1.8}$ NC, can be simultaneously resolved at cryogenic temperature. Our findings thus point to a fascinating scenario in which a semiconductor nanostructure can be further divided into multiple quantum-light sources, the interaction and manipulation of which will promote novel photophysics to facilitate their potential applications in quantum information technologies.

KEYWORDS: mixed-halide perovskite, nanocrystal, nanodomain, discrete elemental distribution, quantum-light source
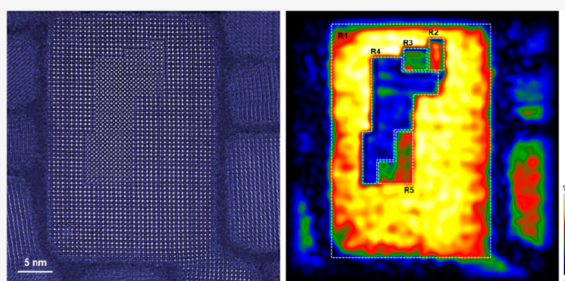
Semiconductor lead-halide perovskites of $APbX_3$, with A being $CH_3NH_3^+$ (MA^+), $HC(NH_2)_2^+$ (FA^+), or Cs^+ and X being I^-, Br^-, or Cl^-, have attracted a great deal of attention in research owing to their superior performance in solar cells,[1−3] light-emitting diodes,[4−6] and lasers.[7−9] Via combination of different types of halide anions with a specific ratio, the as-synthesized lead mixed-halide perovskites can possess a bandgap energy at almost any position in the visible range, thus greatly enhancing the light absorption and emission capabilities of the optoelectronic devices described above.[7,10,11] However, the further advancement of lead mixed-halide perovskites, mainly in the form of $APbBr_xI_{3−x}$ ($0 < x < 3$), is currently hindered by the phase segregation effect due to the formation of Br- and I-rich regions upon light illumination.[12,13] So far, several critical ingredients have been shown to be necessary for the occurrence of phase segregation, such as the driving force provided by local electric fields,[14−16] the migration of I^- anions through lattice vacancies,[17−19] and their final arrival at energetically preferred regions. As revealed from elemental distribution mapping[20] and spatial cathodoluminescence imaging[21] measurements, these regions should correspond to I-rich nanodomains that are more capable of capturing photogenerated holes because of their lower valence-band edges.[20−22] The hole-lattice coupled quasiparticle of the large polaron[23] is then formed to induce excessive strain

energy, which would be released by attracting (repelling) the surrounding I^- (Br^-) anions with the subsequent growth of the nanodomain into a larger I-rich region.[24,25] To pursue the suppression of the phase segregation effect for an improved stability of relevant device operations,[26,27] such an inhomogeneous distribution of halide anions should be avoided by judiciously designing the synthesis protocols. On the contrary, the possible existence of localized nanodomains has rare equivalents in traditional semiconductor nanostructures, rendering lead mixed-halide perovskites a unique platform for exploring novel classical and quantum optical properties.

Here we have synthesized lead mixed-halide perovskite nanocrystals (NCs) of $CsPbBr_{1.2}I_{1.8}$ and probed their intrinsic structure−property relationships by combining annular dark-field scanning transmission electron microscopy (ADF-STEM) imaging and single-particle spectroscopic measurements. It is universal that multiple nanodomains are present inside a single
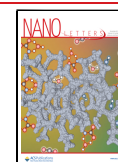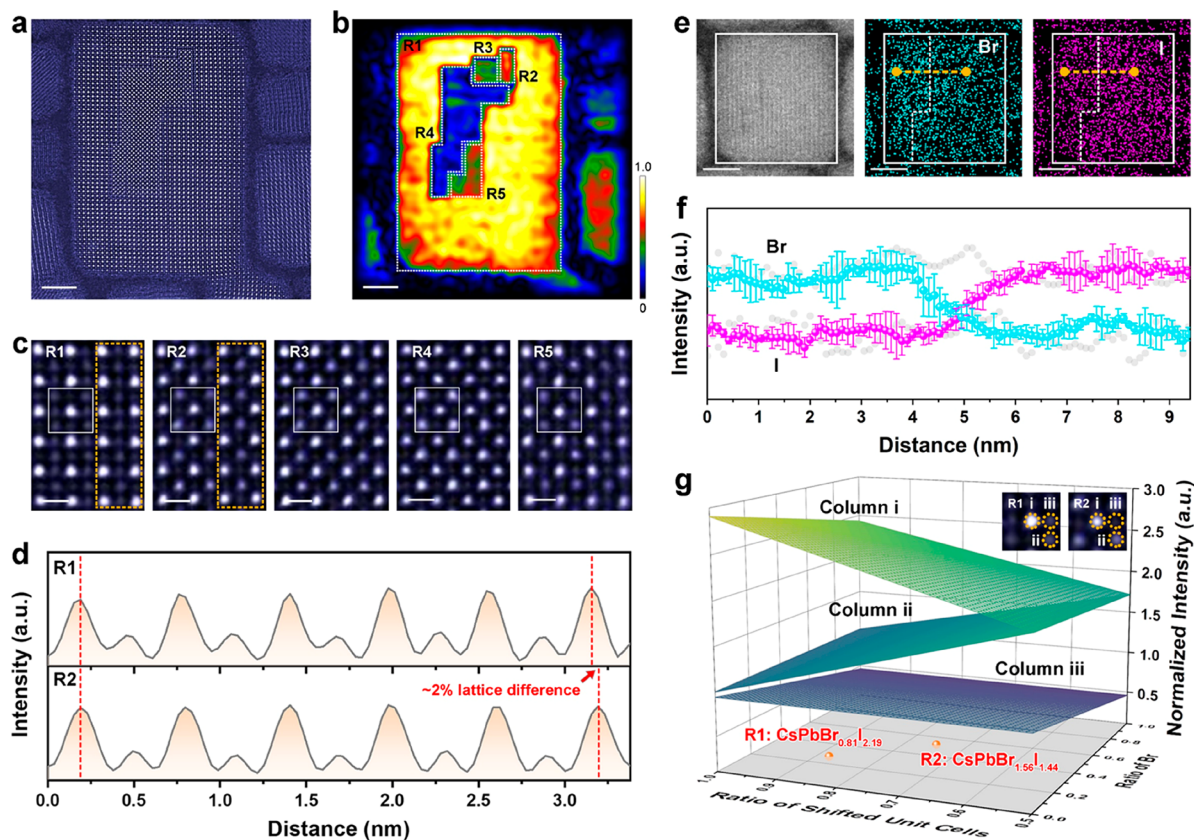
Figure 1. Discrete elemental distributions in single CsPbBr$_{1.2}$I$_{1.8}$ NCs. (a) ADF-STEM image and (b) normalized amplitude map for the (100) reciprocal lattice vector of a typical CsPbBr$_{1.2}$I$_{1.8}$ NC, showing the existence of five nanodomains marked by R1−R5. (c) Atomic-resolution ADF-STEM images for the R1−R5 nanodomains in panel b, where their respective unit cells are highlighted by the white squares. (d) Line intensity profiles of the atom columns highlighted by the orange rectangles in panel c for the R1 and R2 nanodomains. (e) ADF-STEM (left panel) and EDS mapping (right two panels) images for a single CsPbBr$_{1.2}$I$_{1.8}$ NC with the R1 and R2 nanodomains separated by the white dashed lines. (f) EDS intensity scans along the yellow dashed lines in panel e, showing the relative changes in Br and I compositions across the nanodomain boundary. (g) Quantitative composition analysis of the R1 and R2 nanodomains in panel b based on Z-contrast intensity of the ADF-STEM image, confirming their respective compositions of CsPbBr$_{0.81}$I$_{2.19}$ and CsPbBr$_{1.56}$I$_{1.44}$. The inset shows the highlighted atom columns adopted in the calculations. The scale bars are 5 nm in panels a, b, e and 0.5 nm in panel c.

CsPbBr$_{1.2}$I$_{1.8}$ NC with discrete distributions of the Br and I elements, as a result of the abundant Ruddlesden−Popper (RP)-like stacking faults that protect this pre-segregated condition. At a cryogenic temperature of 4 K, photoluminescence (PL) peaks emitted from these nanodomains can be simultaneously observed, each of which possesses a single-photon emission feature due to the strong quantum confinement. This marks the unprecedented formation of multiple quantum dots (QDs) inside a single semiconductor nanostructure, whose mutual interactions are manifested by the correlated variations in their PL intensities and wavelengths.

According to a standard procedure reported previously[15] (see the Experimental Section in the Supporting Information), the cuboid CsPbBr$_{1.2}$I$_{1.8}$ NCs are chemically synthesized with a solution PL peak of ∼620 nm (Figure S1) and an edge length of ∼10−20 nm estimated from the ADF-STEM measurement (Figure S2). As revealed further from the ADF-STEM image (Figure S2), two types of CsPbBr$_{1.2}$I$_{1.8}$ NCs can be resolved with the perfect cubic perovskite lattice and the additional existence of plane defects. For a representative CsPbBr$_{1.2}$I$_{1.8}$ NC displayed in Figure 1a, these plane defects are manifested as black lines that divide it into several nanodomains, each of which has a consistent lattice structure and orientation

according to the fast Fourier transform (FFT) measurement (Figure S3). By means of the geometry phase analysis (GPA) method,[28] we can obtain a normalized amplitude map for the (100) reciprocal lattice vector (Figure 1b and Figure S4), where five nanodomains denoted by R1−R5 are well-identified due to their unequal contributions to the shared (100) spot. The plane defects or black lines delimiting these nanodomain boundaries can be classified into RP-like stacking faults in the manner of $1/2a\langle 111 \rangle$ shifting (a, lattice constant) of two adjacent unit cells,[29,30] as evidenced by the atom model and the simulation results for the ADF-STEM image (Figure S5). The atomic structure for each nanodomain maintains an identical square lattice, while distinct projection intensities of the atom columns can be differentiated inside a single unit cell (Figure 1c). Meanwhile, the line intensity profiles of the highlighted atom columns in Figure 1c reveal a lattice difference of ∼2% between the R1 and R2 nanodomains (Figure 1d), which is an impossible-to-ignore transformation of the crystal structure. As detailed in Table S1, this kind of lattice difference is ubiquitously observed among the R1−R5 nanodomains, implying the existence of local compositional or stacking variations.

Energy dispersive X-ray spectroscopy (EDS) is performed for the composition analysis of single CsPbBr$_{1.2}$I$_{1.8}$ NCs with
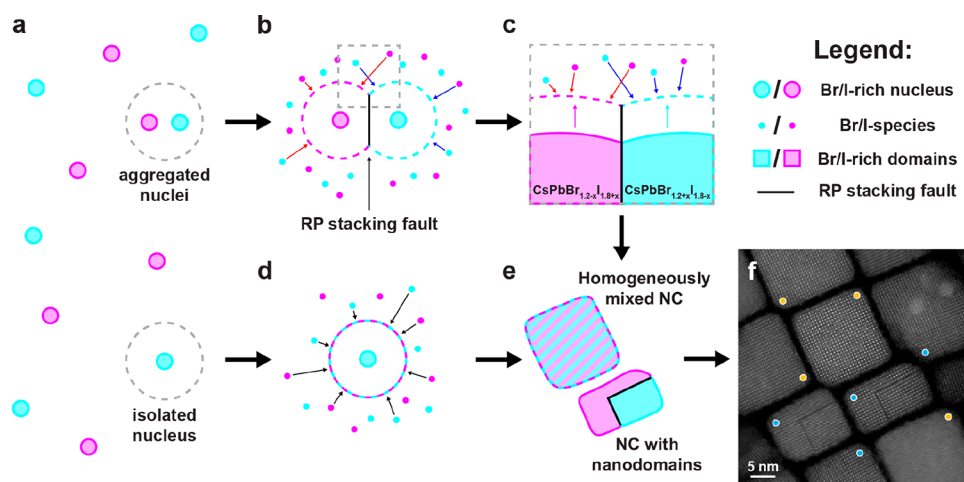
Figure 2. Growth mechanism of $CsPbBr_{1.2}I_{1.8}$ NCs. (a) Inhomogeneous growth in solution, resulting in both isolated and aggregated nuclei. (b) Growth of two aggregated nuclei with enriched Br and I compositions. (c) Emergence of a RP stacking fault across the boundary between two nanodomains with different halide compositions. (d) Growth of an isolated nucleus to which both I and Br species can be attached. (e) One $CsPbBr_{1.2}I_{1.8}$ NC with a homogeneously mixed composition and the other with two nanodomains of different compositions separated by a RP stacking fault. (f) ADF-STEM images of $CsPbBr_{1.2}I_{1.8}$ NCs showing the coexistence of two types of NCs, one with perfect lattices (highlighted by the yellow circles) and the other with planar RP defects (highlighted by the blue circles).
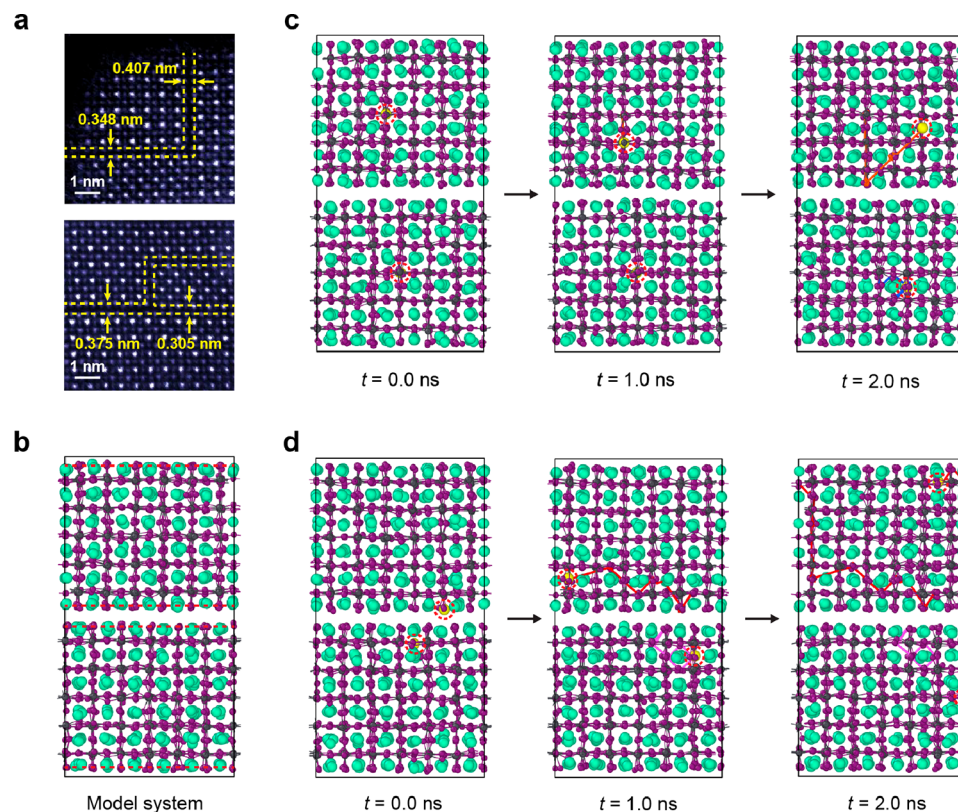
Figure 3. Atomistic details of Ruddledsen−Popper (RP) grain boundaries in an all-inorganic halide perovskite. (a) Atomic-resolution STEM image showing RP grain boundaries (yellow dashed lines) with different widths in two single $CsPbBr_{1.2}I_{1.8}$ NCs. (b) Snapshot of a model system for perovskite grains separated by RP defects as simulated at 500 K. The RP grain boundaries are highlighted with the red dashed lines. (c) Snapshots of the migration of two iodide vacancies initialized in the bulk of $CsPbI_3$ grains. (d) Snapshots of the migration of two iodide vacancies initialized at the surface of $CsPbI_3$ grains. The position of each iodide vacancy is indicated with a yellow sphere, while its initial position is highlighted with a red dashed circle. The time evolutions of defect trajectories are indicated by the orange, blue, red, and pink solid lines, each of which has a resolution of 5 ps.

plane defects, which are found to solely consist of the Cs, Pb, Br, and I elements (Figure S6), albeit with an inhomogeneous distribution of the latter two. As shown for a representative $CsPbBr_{1.2}I_{1.8}$ NC in Figure 1e, a steplike boundary (highlighted by the white dashed line) divides it into the R1 and R2 nanodomains, with R1 possessing slightly stronger Br and weaker I signals than R2. The element line scans plotted in Figure 1f further indicate the tendency of varied Br and I
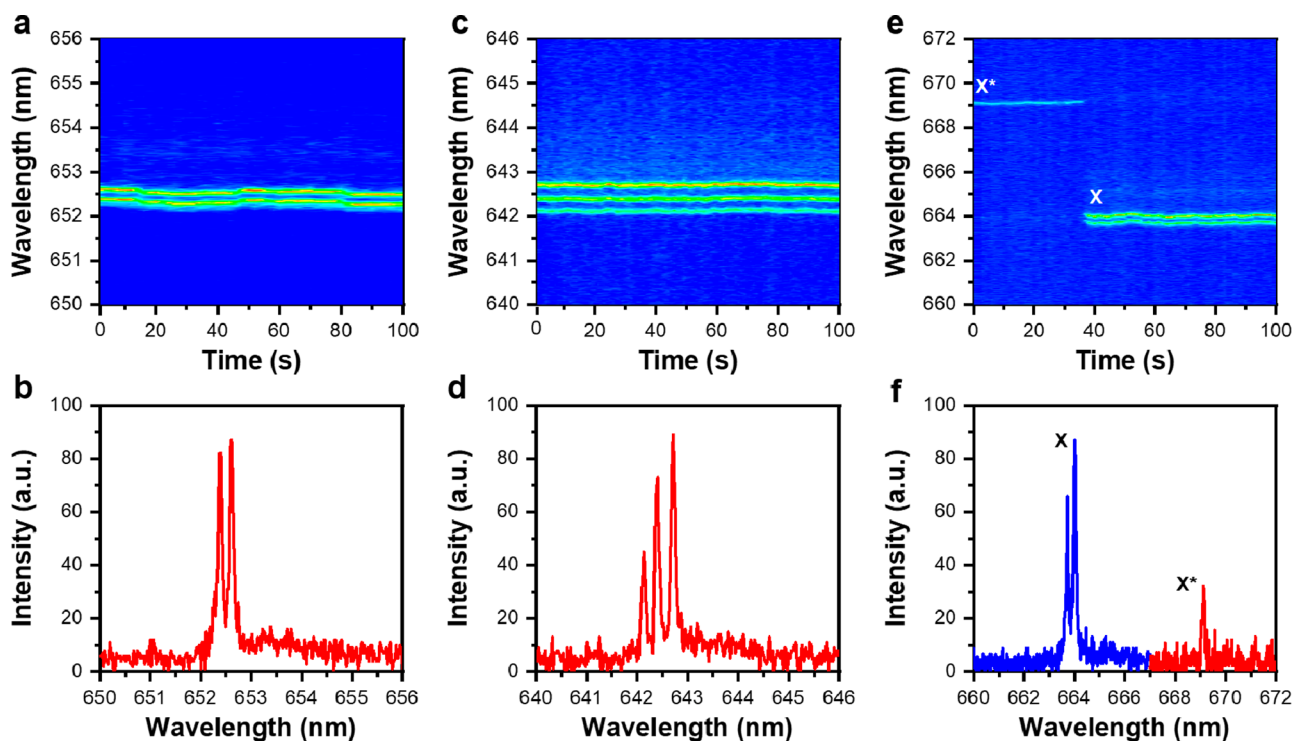
Figure 4. One set of PL peaks measured at 4 K for single $CsPbBr_{1.2}I_{1.8}$ NCs. (a) Time-dependent spectral image measured for a single $CsPbBr_{1.2}I_{1.8}$ NC emitting doublet peaks. (b) PL spectrum of this single $CsPbBr_{1.2}I_{1.8}$ NC extracted from panel a at 1 s. (c) Time-dependent spectral image measured for a single $CsPbBr_{1.2}I_{1.8}$ NC emitting triplet peaks. (d) PL spectrum of this single $CsPbBr_{1.2}I_{1.8}$ NC extracted from panel c at 1 s. (e) Time-dependent spectral image measured for a single $CsPbBr_{1.2}I_{1.8}$ NC, showing the transition from a single peak of charged excitons (X*) to the doublet peaks of neutral excitons (X) at 37 s. (f) PL spectrum of this single $CsPbBr_{1.2}I_{1.8}$ NC with X* and X peaks extracted from panel e at 1 and 40 s, respectively. In the optical measurements described above, each single $CsPbBr_{1.2}I_{1.8}$ NC is excited at ~5 W/cm^2 by a 532 nm pulsed laser.

concentrations, verifying the uniform elemental distribution within each nanodomain as well as the sharp elemental transition at the nanodomain boundary (see Figure S7 for similar results from another NC). The observations described above, along with the lattice difference shown in Figure 1d, naturally lead to the conclusion that the R1 and R2 nanodomains each possess a fixed and isolated ratio between the Br and I elements. Consequently, it is necessary for us to quantitatively determine the inherent compositions for different nanodomains inside a single NC from the Z-contrast ADF-STEM images (Z, the atomic number), such as R1 and R2 in Figure 1b as an example. In Figure 1g, we plot the theoretical intensities of three inequivalent atom columns (i−iii, highlighted in the insets) versus the ratios of Br atoms and shifted unit cells (see the Experimental Section and Figures S8 and S9). Through the statistical analysis of the experimental intensities, the ratios of Br atoms and shifted unit cells are calculated to be 0.27 and 0.88 for the R1 nanodomain, in contrast to the values of 0.52 and 0.75 for the R2 nanodomain. As such, they correspond to the compositions of $CsPbBr_{0.81}I_{2.19}$ and $CsPbBr_{1.56}I_{1.44}$ (see Figure S10 for similar composition analysis on another single NC), respectively, which are consistent with the larger lattice constant of the R1 nanodomain relative to that of the R2 nanodomain[31,32] (see Figure S11 for the statistics on the lattice constants of different nanodomains).

To rationalize the mechanism of formation of the unique structures identified above, we make use of classical nucleation theory to describe the growth process of perovskite NCs.[33] When the preheated $PbI_2/PbBr_2$ (160 °C) and Cs oleate (120 °C) precursor solutions were mixed, perovskite nuclei with diverse compositions, i.e., Br- and I-rich relative to the nominal Br/I ratio of 1.2/1.8, form throughout the solution. As depicted in Figure 2a, these nuclei can be aggregated in a cluster or in just an isolated form. In the clustered case shown in Figure 2b, the Br- and I-rich nuclei can be found in close proximity, and as a result of the rapid growth,[10] they coalesce into one single structure. To release the large amount of strain that results from lattice mismatch, RP stacking faults emerge across the interfaces among different nuclei. Via preferential accumulation of the same type of halide ions at each side of the interface, the neighboring nuclei continue to grow together with the RP stacking fault (Figure 2c). On the contrary, in the isolated case shown in Figure 2d, the single nucleus grows through the addition of both Br and I species from its direct environment.[10,33] As a result of the two separate growth routes mentioned above (see the schematic in Figure 2e), two types of perovskite NCs are eventually formed with a homogeneous mixed-halide composition and the planar RP defects separating nanodomains with discrete mixed-halide compositions (see the STEM image in Figure 2f).

Interestingly, the STEM image in Figure 3a shows that a majority of these RP grain boundaries have CsX (X = I or Br) terminations at both sides.[34] This CsX termination was previously identified as the most stable surface in $CsPbI_3$, because of the intact Pb−I bond and the inhibited migration of halide species due to the steric hindrance effect of Cs species.[35] Using large-scale molecular dynamics (MD) simulations (see the Theoretical Section in the Supporting Information) of a model system in Figure 3b, we reveal how the existence of RP stacking faults influences the migration pathways of nearby halide vacancies in panels c and d of Figure 3. Halide defects
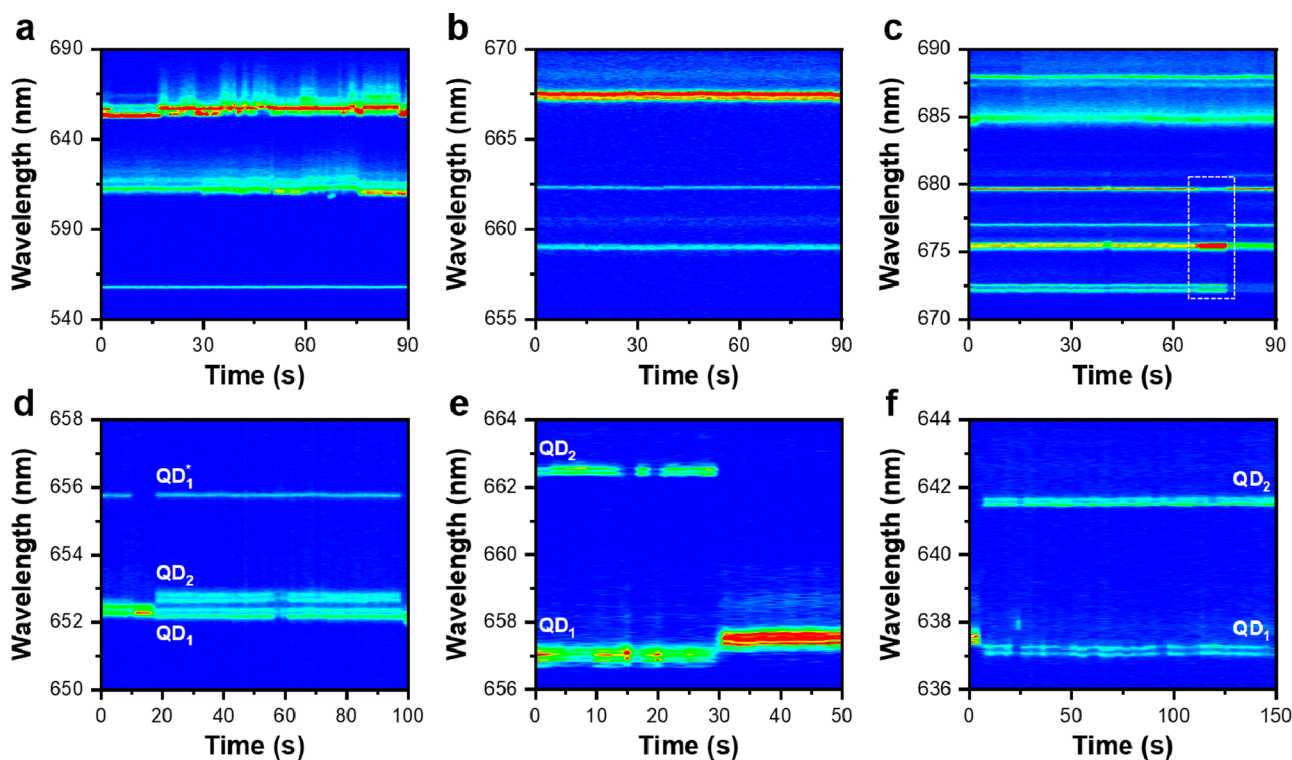
Figure 5. Multiple sets of PL peaks measured at 4 K for single $CsPbBr_{1.2}I_{1.8}$ NCs. (a and b) Time-dependent spectral image measured for two single $CsPbBr_{1.2}I_{1.8}$ NCs with three sets of PL peaks at the wavelength ranges of 540−690 and 655−670 nm, respectively. (c) Time-dependent spectral image measured for a single $CsPbBr_{1.2}I_{1.8}$ NC with six sets of PL peaks in the wavelength range of 670−690 nm. The dotted white box marks out four sets of PL peaks with correlated intensity changes during the time period of 67−75 s. (d) Time-dependent spectral image measured for a single $CsPbBr_{1.2}I_{1.8}$ NC with the optical emissions from QD_1, QD_2, and QD_1^*. (e and f) Time-dependent spectral images measured for another two single $CsPbBr_{1.2}I_{1.8}$ NCs each with optical emissions from QD_1 and QD_2. In the optical measurements described above, each single $CsPbBr_{1.2}I_{1.8}$ NC is excited at ∼5 W/cm² by a 488 nm CW laser.

are generally very mobile, with the ability to hop between lattice sites at time scales as short as 10 ps; they occasionally remain close to their initial positions for as long as a few nanoseconds. Regardless of the starting point (in the bulk or near the RP gain boundary) and the mobility of the halide defects (hopping or stationary), no halide ions are found to migrate across the RP grain boundaries. This confirms that the exchange of halide ions between the nanodomains is prevented once such RP grain boundaries are formed, and therefore, each of their final compositions is locked after the internal ion exchange and migration processes.

After the structural characterizations described above and associated theoretical modeling, we next explore how the optical properties of a single $CsPbBr_{1.2}I_{1.8}$ NC are influenced by the pre-segregated nanodomains at a cryogenic temperature of 4 K. In this case, the sample substrate is attached to the coldfinger of a helium-free cryostat and a single $CsPbBr_{1.2}I_{1.8}$ NC is excited at ∼5 W/cm² by either a continuous-wave (CW) 488 nm or a pulsed 532 nm laser (see the Experimental Section in the Supporting Information). For ∼90 of the total ∼130 single $CsPbBr_{1.2}I_{1.8}$ NCs studied in our experiment, we observe either a single peak, doublet peaks, or triplet peaks as the PL spectrum, due to the existence of bright neutral exciton fine structures.[36−39] Panels a and b of Figure 4 show the time-dependent spectral image and the corresponding PL spectrum measured for a single $CsPbBr_{1.2}I_{1.8}$ NC emitting doublet peaks with a fine-structure splitting of ∼677 μeV. Similarly, the time-dependent spectral image and the corresponding PL spectrum are plotted in panels c and d of Figure 4 for a single

$CsPbBr_{1.2}I_{1.8}$ NC emitting triplet peaks, with a fine-structure splitting of ∼878 μeV that is defined as the average value of the two nearby energy separations. It is also observed that a single $CsPbBr_{1.2}I_{1.8}$ NC can be photocharged sometimes, leading to a single-step transition between the doublet or triplet peaks from neutral excitons and a single peak from charged excitons.[37,38] This is representatively shown in the time-dependent spectral image and the corresponding PL spectrum plotted in panels e and f, respectively, of Figure 4, where the single peak of charged excitons in a single $CsPbBr_{1.2}I_{1.8}$ NC stops emitting after laser excitation for ∼37 s, with the accompanying emergence of doublet peaks from neutral excitons.

The optical properties shown in Figure 4 are on par with those already reported for single-halide $CsPbBr_3$ and $CsPbI_3$ NCs,[37,38] implying that the exciton quantum confinement is mainly dictated by the whole spatial volume of a single $CsPbBr_{1.2}I_{1.8}$ NC without the existence of internal nano-domains. In stark contrast, the remaining ∼40 of the total of ∼130 single $CsPbBr_{1.2}I_{1.8}$ NCs studied in our experiment exhibit a PL spectrum containing multiple sets of PL peaks that are jointly contributed by the pre-segregated nanodomains (see Table S2 for their statistical PL properties). As Figure 5a shows from the time-dependent spectral image measured for a single $CsPbBr_{1.2}I_{1.8}$ NC, there are three sets of PL peaks with their central wavelengths at ∼557.93, ∼615.83, and ∼657.88 nm. In Figure S12, we plot the time-dependent spectral images measured for four more single $CsPbBr_{1.2}I_{1.8}$ NCs each emitting multiple sets of PL peaks across the wavelength range of 540− 690 nm. The PL peaks below 600 nm are emitted from those

Br-rich nanodomains of single $CsPbBr_{1.2}I_{1.8}$ NCs, and possibly due to their overlap with the continuum absorption states of other I-rich nanodomains, they are normally associated with weak intensities to imply the occurrence of Förster-type exciton transfers. In Figure 5b, we plot the time-dependent spectral image measured for another single $CsPbBr_{1.2}I_{1.8}$ NC, where three sets of PL peaks can be resolved at the central wavelengths of ~659.02, ~662.28, and ~667.46 nm. For one more single $CsPbBr_{1.2}I_{1.8}$ NC whose time-dependent spectral image is plotted in Figure 5c, up to six sets of PL peaks can be simultaneously resolved in the wavelength range of 670−690 nm. For these multiple sets of PL peaks emitted from a single $CsPbBr_{1.2}I_{1.8}$ NC with close central wavelengths, the discrete nature in band-edge emission and absorption states of the corresponding nanodomains makes it impossible for them to interact with each other via the resonant carrier tunneling and the nonresonant exciton transfer processes.

The broad wavelength distribution of the PL peaks emitted by a single $CsPbBr_{1.2}I_{1.8}$ NC, as observed from the three time-dependent spectral images plotted in Figure 5a−c, is consistent with the different Br:I ratios among its internal nanodomains. Because the size of an individual nanodomain is normally smaller than the Bohr diameters of perovskite $CsPbBr_3$ and $CsPbI_3$,[10] we speculate that its PL peak should be additionally influenced by the quantum-confinement effect. Moreover, due to compositional differences between neighboring nanodomains, the dielectric-confinement effect might also play a role in determining their respective PL peaks. According to the second-order photon correlation measurements shown in Figure S13, each of the multiple sets of PL peaks emitted by a single $CsPbBr_{1.2}I_{1.8}$ NC is associated with a single-photon emission feature. Consequently, it is reasonable to assign multiple nanodomains inside a single $CsPbBr_{1.2}I_{1.8}$ NC to closely packed QDs. In Figure S14a, we plot two sets of PL peaks emitted by a single $CsPbBr_{1.2}I_{1.8}$ NC, and as one can see from the PL decay curves shown in Figure S14b, their corresponding QDs have quite similar exciton recombination dynamics with single-exponential lifetimes of ~0.54 and ~0.66 ns.

As marked by the white dotted rectangle in Figure 5c for a single $CsPbBr_{1.2}I_{1.8}$ NC, the four PL peaks with close central wavelengths show correlated changes in their intensities during the time period of ~67−75 s. In Figure 5d, we plot the time-dependent spectral image measured for another single $CsPbBr_{1.2}I_{1.8}$ NC emitting two sets of PL peaks at the very beginning, which are marked by QD_1 and QD_1^* with central wavelengths of ~652.36 and ~655.76 nm, respectively. The QD_1^* peak switches off at ~10 s with the associated brightening of the broad QD_1 peak so that they should be contributed by the charged and neutral excitons of a single QD. The QD_1^* peak shows up again at ~18 s, while the QD_1 peak shifts slightly to the blue side and evolves into doublet peaks with a central wavelength of ~652.26 nm. Meanwhile, additional doublet PL peaks of QD_2 appear at the central wavelength of ~652.71 nm, and they stop emitting at ~98 s together with the QD_1^* peak, in accordance with a slight shift of the QD_1 doublet peaks to the blue side. In panels e and f of Figure 5, we provide the time-dependent spectral images measured for two more single $CsPbBr_{1.2}I_{1.8}$ NCs, whose respective QD_1 and QD_2 peaks are also correlated with each other in terms of the intensity and wavelength variations (see Figure S15 for more examples). These observations strongly suggest that the multiple QDs inside a single $CsPbBr_{1.2}I_{1.8}$ NC

can compete with each other for the capture of photogenerated excitons, and it is also possible for the transient electric field caused by environmental charge movement[40] to exert synchronous influences on their exciton recombination dynamics.

To summarize, we have synthesized mixed-halide perovskite $CsPbBr_xI_{3-x}$ NCs with a nominal x value of 1.2 and confirmed from the ADF-STEM measurements that they can each contain multiple nanodomains separated by the RP-like plane defects and with different compositional ratios of Br^- to I^- anions. Of special note is the fact that these pre-segregated nanodomains can be universally detected from the $CsPbBr_xI_{3-x}$ NCs synthesized with other x values, including $CsPbBr_{2.1}I_{0.9}$, $CsPbBr_{1.8}I_{1.2}$, $CsPbBr_{1.5}I_{1.5}$, and $CsPbBr_{0.9}I_{2.1}$ (see ADF-STEM images in Figures S16 and S17). The formation of such novel nanodomains with discrete elemental distributions should be a direct consequence of the size difference between Br^- (~196 pm) and I^- (~220 pm) anions,[41,42] which would induce local lattice stress in the perovskite octahedron skeleton. This local lattice stress can be effectively released through the formation of isolated nanodomains with varied plane-to-plane distances or widths of the bridging boundaries (Figure S18) in the form of RP stacking faults. Our MD simulations reveal that the RP grain boundaries act as barriers to halide migration during and after the growth of these nanodomains, thus preserving the discrete elemental distributions of the Br^- and I^- anions. In the context that the inhomogeneous distributions of halide anions are now routinely reported in bulk mixed-halide perovskites,[20,21,24,25] the findings described above have brought such a concept of pre-segregation to their nanostructured counterparts.

As revealed from our 4 K optical measurement on a single $CsPbBr_{1.2}I_{1.8}$ NC, the photogenerated excitons can be captured separately by the internal nanodomains (see the schematic diagram in Figure S19) to yield multiple sets of PL peaks each possessing a single-photon emission feature. In this sense, all of the nanodomains inside a single $CsPbBr_{1.2}I_{1.8}$ NC can be jointly treated as a collection of single QDs, whose spatial distributions are defined by the RP-like boundaries separating different halide compositions. These multiple QDs are not simply assembled but have mutual interactions with correlated PL intensity and wavelength changes, and the coupling strengths can be surely manipulated by optimizing the synthesis conditions and applying external stimuli such as an electric field. Overall, the findings presented in this report have significantly expanded the scope of material growth in that a single semiconductor nanostructure can now be further divided into multiple functional units, which can be utilized to explore fundamental molecular-like many-body physics toward novel applications in both classical optoelectronics and quantum information technologies.

■ ASSOCIATED CONTENT

ⓢ Supporting Information

The Supporting Information is available free of charge at https://pubs.acs.org/doi/10.1021/acs.nanolett.3c03761.

> Experimental and theoretical sections, absorption and PL spectra, ADF-STEM images, fast Fourier transform (FFT) measurement, geometry phase analysis (GPA), atomic models and simulated results for the ADF-STEM image, experimental lattice constants, EDS analysis, quantitative calculations of the nanodomain composi-

tions, misalignment of atom columns along the incident beam direction, discrete elemental distributions in another single $CsPbBr_{1.2}I_{1.8}$ NC, statistics of the lattice constants of different nanodomains, statistics of the nanodomain PL properties, time-dependent spectral images, second-order photon correlation measurements, PL decay measurements, correlated changes of PL intensities and wavelengths, analysis of the widths of nanodomain boundaries, schematic diagram for the optical emission, ADF-STEM image taken under long-term electron beam irradiation, postprocessing methods of the ADF-STEM images, validation of the simulated RP grain boundary systems, and details of the defect behavior simulations (PDF)

■ AUTHOR INFORMATION

Corresponding Authors

Chao Zhu − *SEU-FEI Nano-Pico Center, Key Laboratory of MEMS of Ministry of Education, and School of Electronic Science and Engineering, Southeast University, Nanjing 210096, China;* orcid.org/0000-0001-6383-3665; Email: phczhu@seu.edu.cn

Shuxia Tao − *Materials Simulation & Modelling, Department of Applied Physics, Eindhoven University of Technology, Eindhoven 5600 MB, The Netherlands;* orcid.org/0000-0002-3658-8497; Email: S.X.Tao@Tue.nl

Min Xiao − *National Laboratory of Solid State Microstructures, School of Physics, and Collaborative Innovation Center of Advanced Microstructures, Nanjing University, Nanjing 210093, China; Department of Physics, University of Arkansas, Fayetteville, Arkansas 72701, United States;* Email: mxiao@uark.edu

Xiaoyong Wang − *National Laboratory of Solid State Microstructures, School of Physics, and Collaborative Innovation Center of Advanced Microstructures, Nanjing University, Nanjing 210093, China;* orcid.org/0000-0003-1147-0051; Email: wxiaoyong@nju.edu.cn

Authors

Jinqiu Liu − *National Laboratory of Solid State Microstructures, School of Physics, and Collaborative Innovation Center of Advanced Microstructures, Nanjing University, Nanjing 210093, China*

Mike Pols − *Materials Simulation & Modelling, Department of Applied Physics, Eindhoven University of Technology, Eindhoven 5600 MB, The Netherlands;* orcid.org/0000-0002-1068-9599

Zhen Zhang − *National Laboratory of Solid State Microstructures, School of Physics, and Collaborative Innovation Center of Advanced Microstructures, Nanjing University, Nanjing 210093, China*

Fengrui Hu − *College of Engineering and Applied Sciences and MOE Key Laboratory of Intelligent Optical Sensing and Manipulation, Nanjing University, Nanjing 210093, China;* orcid.org/0000-0002-8268-7373

Lin Wang − *Key Laboratory of Flexible Electronics (KLOFE) and Institute of Advanced Materials (IAM), Nanjing Tech University, Nanjing 211816, China;* orcid.org/0000-0003-3033-4792

Chunfeng Zhang − *National Laboratory of Solid State Microstructures, School of Physics, and Collaborative Innovation Center of Advanced Microstructures, Nanjing*

University, Nanjing 210093, China; orcid.org/0000-0001-9030-5606

Zheng Liu − *School of Materials Science and Engineering, Nanyang Technological University, Singapore 639798;* orcid.org/0000-0002-8825-7198

Complete contact information is available at:
https://pubs.acs.org/10.1021/acs.nanolett.3c03761

Author Contributions

@J.L., C.Z., M.P. and Z.Z. contributed equally to this work.

Notes

The authors declare no competing financial interest.

■ REFERENCES

(1) Kojima, A.; Teshima, K.; Shirai, Y.; Miyasaka, T. Organometal halide perovskites as visible-light sensitizers for photovoltaic cells. *J. Am. Chem. Soc.* **2009**, *131*, 6050−6051.

(2) Liu, M.; Johnston, M. B.; Snaith, H. J. Efficient planar heterojunction perovskite solar cells by vapour deposition. *Nature* **2013**, *501*, 395−398.

(3) Zhou, H.; Chen, Q.; Li, G.; Luo, S.; Song, T.-B.; Duan, H.-S.; Hong, Z.; You, J.; Liu, Y.; Yang, Y. Interface engineering of highly efficient perovskite solar cells. *Science* **2014**, *345*, 542−546.

(4) Tan, Z. K.; Moghaddam, R. S.; Lai, M. L.; Docampo, P.; Higler, R.; Deschler, F.; Price, M.; Sadhanala, A.; Pazos, L. M.; Credgington, D.; Hanusch, F.; Bein, T.; Snaith, H. J.; Friend, R. H. Bright light-emitting diodes based on organometal halide perovskite. *Nat. Nanotechnol.* **2014**, *9*, 687−692.

(5) Lin, K.; Xing, J.; Quan, L. N.; de Arquer, F. P. G.; Gong, X.; Lu, J.; Xie, L.; Zhao, W.; Zhang, D.; Yan, C.; Li, W.; Liu, X.; Lu, Y.; Kirman, J.; Sargent, E. H.; Xiong, Q.; Wei, Z. Perovskite light-emitting diodes with external quantum efficiency exceeding 20%. *Nature* **2018**, *562*, 245−248.

(6) Zhao, X.; Tan, Z.-K. Large-area near-infrared perovskite light-emitting diodes. *Nat. Photonics* **2020**, *14*, 215−218.

(7) Xing, G.; Mathews, N.; Lim, S. S.; Yantara, N.; Liu, X.; Sabba, D.; Grätzel, M.; Mhaisalkar, S.; Sum, T. C. Low-temperature solution-processed wavelength-tunable perovskites for lasing. *Nat. Mater.* **2014**, *13*, 476−480.

(8) Yakunin, S.; Protesescu, L.; Krieg, F.; Bodnarchuk, M. I.; Nedelcu, G.; Humer, M.; De Luca, G.; Fiebig, M.; Heiss, W.; Kovalenko, M. V. Low-threshold amplified spontaneous emission and lasing from colloidal nanocrystals of caesium lead halide perovskites. *Nat. Commun.* **2015**, *6*, 8056.

(9) Zhang, N.; Fan, Y.; Wang, K.; Gu, Z.; Wang, Y.; Ge, L.; Xiao, S.; Song, Q. All-optical control of lead halide perovskite microlasers. *Nat. Commun.* **2019**, *10*, 1770.

(10) Protesescu, L.; Yakunin, S.; Bodnarchuk, M. I.; Krieg, F.; Caputo, R.; Hendon, C. H.; Yang, R. X.; Walsh, A.; Kovalenko, M. V. Nanocrystals of cesium lead halide perovskites ($CsPbX_3$, X = Cl, Br, and I): novel optoelectronic materials showing bright emission with wide color gamut. *Nano Lett.* **2015**, *15*, 3692−3696.

(11) Beal, R. E.; Slotcavage, D. J.; Leijtens, T.; Bowring, A. R.; Belisle, R. A.; Nguyen, W. H.; Burkhard, G. F.; Hoke, E. T.; McGehee,

M. D. Cesium lead halide perovskites with improved stability for tandem solar cells. *J. Phys. Chem. Lett.* **2016**, *7*, 746−751.

(12) Hoke, E. T.; Slotcavage, D. J.; Dohner, E. R.; Bowring, A. R.; Karunadasa, H. I.; McGehee, M. D. Reversible photo-induced trap formation in mixed-halide hybrid perovskites for photovoltaics. *Chem. Sci.* **2015**, *6*, 613−617.

(13) Brennan, M. C.; Ruth, A.; Kamat, P. V.; Kuno, M. Photoinduced anion segregation in mixed halide perovskites. *Trends Chem.* **2020**, *2*, 282−301.

(14) Belisle, R. A.; Bush, K. A.; Bertoluzzi, L.; Gold-Parker, A.; Toney, M. F.; McGehee, M. D. Impact of surfaces on photoinduced halide segregation in mixed-halide perovskites. *ACS Energy Lett.* **2018**, *3*, 2694−2700.

(15) Zhang, H.; Fu, X.; Tang, Y.; Wang, H.; Zhang, C.; Yu, W. W.; Wang, X.; Zhang, Y.; Xiao, M. Phase segregation due to ion migration in all-inorganic mixed-halide perovskite nanocrystals. *Nat. Commun.* **2019**, *10*, 1088.

(16) Knight, A. J.; Wright, A. D.; Patel, J. B.; McMeekin, D. P.; Snaith, H. J.; Johnston, M. B.; Herz, L. M. Electronic traps and phase segregation in lead mixed-halide perovskite. *ACS Energy Lett.* **2019**, *4*, 75−84.

(17) Eames, C.; Frost, J. M.; Barnes, P. R.; O'Regan, B. C.; Walsh, A.; Islam, M. S. Ionic transport in hybrid lead iodide perovskite solar cells. *Nat. Commun.* **2015**, *6*, 7497.

(18) deQuilettes, D. W.; Zhang, W.; Burlakov, V. M.; Graham, D. J.; Leijtens, T.; Osherov, A.; Bulović, V.; Snaith, H. J.; Ginger, D. S.; Stranks, S. D. Photo-induced halide redistribution in organic-inorganic perovskite films. *Nat. Commun.* **2016**, *7*, 11683.

(19) Ruth, A.; Brennan, M. C.; Draguta, S.; Morozov, Y. V.; Zhukovskyi, M.; Janko, B.; Zapol, P.; Kuno, M. Vacancy-mediated anion photosegregation kinetics in mixed halide hybrid perovskites: coupled kinetic Monte Carlo and optical measurements. *ACS Energy Lett.* **2018**, *3*, 2321−2328.

(20) Gratia, P.; Grancini, G.; Audinot, J.-N.; Jeanbourquin, X.; Mosconi, E.; Zimmermann, I.; Dowsett, D.; Lee, Y.; Grätzel, M.; De Angelis, F.; Sivula, K.; Wirtz, T.; Nazeeruddin, M. K. Intrinsic halide segregation at nanometer scale determines the high efficiency of mixed cation/mixed halide perovskite solar cells. *J. Am. Chem. Soc.* **2016**, *138*, 15821−15824.

(21) Bischak, C. G.; Hetherington, C. L.; Wu, H.; Aloni, S.; Ogletree, D. F.; Limmer, D. T.; Ginsberg, N. S. Origin of reversible photoinduced phase separation in hybrid perovskites. *Nano Lett.* **2017**, *17*, 1028−1033.

(22) Draguta, S.; Sharia, O.; Yoon, S. J.; Brennan, M. C.; Morozov, Y. V.; Manser, J. S.; Kamat, P. V.; Schneider, W. F.; Kuno, M. Rationalizing the light-induced phase separation of mixed halide organic-inorganic perovskites. *Nat. Commun.* **2017**, *8*, 200.

(23) Zhu, X.-Y.; Podzorov, V. Charge carriers in hybrid organic-inorganic lead halide perovskites might be protected as large polarons. *J. Phys. Chem. Lett.* **2015**, *6*, 4758−4761.

(24) Bischak, C. G.; Wong, A. B.; Lin, E.; Limmer, D. T.; Yang, P.; Ginsberg, N. S. Tunable polaron distortions control the extent of halide demixing in lead halide perovskites. *J. Phys. Chem. Lett.* **2018**, *9*, 3998−4005.

(25) Wang, X.; Ling, Y.; Lian, X.; Xin, Y.; Dhungana, K. B.; Perez-Orive, F.; Knox, J.; Chen, Z.; Zhou, Y.; Beery, D.; Hanson, K.; Shi, J.; Lin, S.; Gao, H. Suppressed phase separation of mixed-halide perovskites confined in endotaxial matrices. *Nat. Commun.* **2019**, *10*, 695.

(26) McMeekin, D. P.; Sadoughi, G.; Rehman, W.; Eperon, G. E.; Saliba, M.; Hörantner, M. T.; Haghighirad, A.; Sakai, N.; Korte, L.; Rech, B.; Johnston, M. B.; Herz, L. M.; Snaith, H. J. A mixed-cation lead mixed-halide perovskite absorber for tandem solar cells. *Science* **2016**, *351*, 151−155.

(27) Xu, J.; Boyd, C. C.; Yu, Z. J.; Palmstrom, A. F.; Witter, D. J.; Larson, B. W.; France, R. M.; Werner, J.; Harvey, S. P.; Wolf, E. J.; Weigand, W.; Manzoor, S.; van Hest, M. F. A. M.; Berry, J. J.; Luther, J. M.; Holman, Z. C.; McGehee, M. D. Triple-halide wide-band gap

perovskites with suppressed phase segregation for efficient tandems. *Science* **2020**, *367*, 1097−1104.

(28) Zhu, C.; Yu, M.; Zhou, J.; He, Y.; Zeng, Q.; Deng, Y.; Guo, S.; Xu, M.; Shi, J.; Zhou, W.; Sun, L.; Wang, L.; Hu, Z.; Zhang, Z.; Guo, W.; Liu, Z. Strain-driven growth of ultra-long two-dimensional nano-channels. *Nat. Commun.* **2020**, *11*, 772.

(29) Yu, Y.; Zhang, D.; Yang, P. Ruddlesden-Popper phase in two-dimensional inorganic halide perovskites: a plausible model and the supporting observations. *Nano Lett.* **2017**, *17*, 5489−5494.

(30) Paul, S.; Bladt, E.; Richter, A. F.; Döblinger, M.; Tong, Y.; Huang, H.; Dey, A.; Bals, S.; Debnath, T.; Polavarapu, L.; Feldmann, J. Manganese-doping-induced quantum confinement within host perovskite nanocrystals through Ruddlesden-Popper defects. *Angew. Chem., Int. Ed.* **2020**, *59*, 6794−6799.

(31) He, X.; Qiu, Y.; Yang, S. Fully-inorganic trihalide perovskite nanocrystals: a new research frontier of optoelectronic materials. *Adv. Mater.* **2017**, *29*, 1700775.

(32) Chen, Q.; Wu, J.; Ou, X.; Huang, B.; Almutlaq, J.; Zhumekenov, A. A.; Guan, X.; Han, S.; Liang, L.; Yi, Z.; Li, J.; Xie, X.; Wang, Y.; Li, Y.; Fan, D.; Teh, D. B. L.; All, A. H.; Mohammed, O. F.; Bakr, O. M.; Wu, T.; Bettinelli, M.; Yang, H.; Huang, W.; Liu, X. All-inorganic perovskite nanocrystal scintillators. *Nature* **2018**, *561*, 88−93.

(33) Koscher, B. A.; Bronstein, N. D.; Olshansky, J. H.; Bekenstein, Y.; Alivisatos, A. P. Surface- vs diffusion-limited mechanisms of anion exchange in CsPbBr₃ nanocrystal cubes revealed through kinetic studies. *J. Am. Chem. Soc.* **2016**, *138*, 12065−12068.

(34) Thind, A. S.; Luo, G.; Hachtel, J. A.; Morrell, M. V.; Cho, S. B.; Borisevich, A. Y.; Idrobo, J.-C.; Xing, Y.; Mishra, R. Atomic structure and electrical activity of grain boundaries and Ruddlesden-Popper faults in cesium lead bromide perovskite. *Adv. Mater.* **2019**, *31*, 1805047.

(35) Pols, M.; Hilpert, T.; Filot, I.; van Duin, A. C. T.; Calero, S.; Tao, S. What happens at surfaces and grain boundaries of halide perovskites: insights from reactive molecular dynamics simulations of CsPbI₃. *ACS Appl. Mater. Interfaces* **2022**, *14*, 40841−40850.

(36) Rainò, G.; Nedelcu, G.; Protesescu, L.; Bodnarchuk, M. I.; Kovalenko, M. V.; Mahrt, R. F.; Stöferle, T. Single cesium lead halide perovskite nanocrystals at low temperature: fast single-photon emission, reduced blinking, and exciton fine structure. *ACS Nano* **2016**, *10*, 2485−2490.

(37) Fu, M.; Tamarat, P.; Huang, H.; Even, J.; Rogach, A. L.; Lounis, B. Neutral and charged exciton fine structure in single lead halide perovskite nanocrystals revealed by magneto-optical spectroscopy. *Nano Lett.* **2017**, *17*, 2895−2901.

(38) Yin, C.; Chen, L.; Song, N.; Lv, Y.; Hu, F.; Sun, C.; Yu, W. W.; Zhang, C.; Wang, X.; Zhang, Y.; Xiao, M. Bright-exciton fine-structure splittings in single perovskite nanocrystals. *Phys. Rev. Lett.* **2017**, *119*, No. 026401.

(39) Becker, M. A.; Vaxenburg, R.; Nedelcu, G.; Sercel, P. C.; Shabaev, A.; Mehl, M. J.; Michopoulos, J. G.; Lambrakos, S. G.; Bernstein, N.; Lyons, J. L.; Stoferle, T.; Mahrt, R. F.; Kovalenko, M. V.; Norris, D. J.; Rainò, G.; Efros, A. L. Bright triplet excitons in caesium lead halide perovskites. *Nature* **2018**, *553*, 189−193.

(40) Empedocles, S. A.; Bawendi, M. G. Quantum-confined Stark effect in single CdSe nanocrystallite quantum dots. *Science* **1997**, *278*, 2114−2117.

(41) Shannon, R. D. Revised effective ionic radii and systematic studies of interatomic distances in halides and chalcogenides. *Acta Crystallogr.* **1976**, *A32*, 751−767.

(42) Akkerman, Q. A.; Bladt, E.; Petralanda, U.; Dang, Z.; Sartori, E.; Baranov, D.; Abdelhady, A. L.; Infante, I.; Bals, S.; Manna, L. Fully inorganic Ruddlesden-Popper double Cl-I and triple Cl-Br-I lead halide perovskite nanocrystals. *Chem. Mater.* **2019**, *31*, 2182−2190.